

Dynamos of Giant Planets

F. H. Busse¹ and R. Simitev²

¹Institute of Physics, University of Bayreuth, D95440 Bayreuth, Germany
 email: busse@uni-bayreuth.de

²Department of Mathematics, University of Glasgow, Glasgow G12 8QW, UK
 email: rs@maths.gla.ac.uk

Abstract. Possibilities and difficulties of applying the theory of magnetic field generation by convection flows in rotating spherical fluid shells to the Giant Planets are outlined. Recent progress in the understanding of the distribution of electrical conductivity in the Giant Planets suggests that the dynamo process occurs predominantly in regions of semiconductivity. In contrast to the geodynamo the magnetic field generation in the Giant Planets is thus characterized by strong radial conductivity variations. The importance of the constraint on the Ohmic dissipation provided by the planetary luminosity is emphasized. Planetary dynamos are likely to be of an oscillatory type, although these oscillations may not be evident from the exterior of the planets.

Keywords. Planetary dynamo, convection in rotating spheres, oscillatory dynamos, semi-conducting hydrogen, semi-conducting “ices”

1. Introduction

Even before the Pioneer and Voyager missions evidence for a global Jovian magnetic field had been obtained through the observations of decametric radio waves by Burke & Franklin (1955). The subsequent discoveries of the magnetic fields of Saturn, Uranus and Neptune have been highlights of the exploration of the solar system by space probes. While Jupiter and Saturn possess magnetic fields which are dominated by a dipole part that is nearly aligned with the axis of planetary rotation, Uranus and Neptune exhibit magnetic fields that do not show such an alignment and are also characterized by a strong quadrupolar component. This latter property has been interpreted in earlier papers (Ruzmaikin & Starchenko, 1991; Stanley & Bloxham, 2004) as a result of the thin shell to which the dynamo process is assumed to be confined. This explanation is not entirely convincing, however, since Liu et al. (2006) argue convincingly that the dynamo process in Jupiter and Saturn is also confined to thin fluid shells. As will be pointed out in section 5 magnetic fields without a dominant axis-aligned dipole are a rather common feature of numerical simulations of planetary dynamos.

In the following we shall first briefly introduce the mathematical background for numerical dynamo simulations. At the present stage it appears to be appropriate to introduce only a minimum of physical parameters in order to obtain an overview of the parameter dependence of planetary dynamos. Hence we shall not even consider the compressibility of the fluid in the Giant Planets and restrict the analysis to the Boussinesq approximation. An alternative approach has been used by Evonuk & Glatzmaier (2006) (see also article by Glatzmaier in these Proceedings) where a fairly accurate representation of the compressibility of Jupiter has been attempted.

2. Mathematical Description of Convection Driven Spherical Dynamos

For the equations describing convection driven dynamos in the frame rotating with the angular velocity Ω we use a standard formulation which has also been used for a dynamo benchmark (Christensen et al., 2001). A more general static state will be assumed with the temperature distribution $T_S = T_0 - \beta d^2 r^2 / 2 + \Delta T \eta r^{-1} (1 - \eta)^{-2}$ where η denotes the ratio of inner to outer radius of the spherical shell and d is its thickness. ΔT is the temperature difference between the boundaries in the special case $\beta = 0$. In the case $\Delta T = 0$ the static temperature distribution T_S corresponds to that of a homogeneously heated sphere with the heat source density proportional to the parameter β . The gravity field is given by $\mathbf{g} = -\gamma d \mathbf{r}$ where \mathbf{r} is the position vector with respect to the center of the sphere and r is its length measured in units of d .

In addition to d , the time d^2/ν , the temperature $\nu^2/\gamma\alpha d^4$ and the magnetic flux density $\nu(\mu\varrho)^{1/2}/d$ are used as scales for the dimensionless description of the problem where ν denotes the kinematic viscosity of the fluid, κ its thermal diffusivity, ϱ its density and μ its magnetic permeability. The Boussinesq approximation is used in that ϱ is assumed to be constant except in the gravity term where its temperature dependence given by $\alpha \equiv -(d\varrho/dT)/\varrho = \text{const.}$ is taken into account. The dimensionless equations of motion, the heat equation for the deviation Θ of the temperature field from the static distribution and the equation of magnetic induction thus assume the form

$$\nabla^2 \mathbf{v} + \mathbf{B} \cdot \nabla \mathbf{B} + \mathbf{r} \Theta - \nabla \pi = P^{-1} (\partial_t \mathbf{v} + \mathbf{v} \cdot \nabla \mathbf{v}) + \tau \mathbf{k} \times \mathbf{v} \quad (2.1)$$

$$\nabla \cdot \mathbf{v} = 0 \quad (2.2)$$

$$\nabla^2 \Theta + [R_i + R_e \eta r^{-3} (1 - \eta)^{-2}] \mathbf{r} \cdot \mathbf{v} = P (\partial_t + \mathbf{v} \cdot \nabla) \Theta \quad (2.3)$$

$$P_m (\partial_t + \mathbf{v} \cdot \nabla) \mathbf{B} + \nabla \times \left(\frac{\lambda}{\lambda_0} \nabla \times \mathbf{B} \right) = P_m \mathbf{B} \cdot \nabla \mathbf{v} \quad (2.4)$$

where \mathbf{k} is the unit vector in the direction of the axis of rotation and where $\nabla \pi$ includes all terms that can be written as gradients. The Rayleigh numbers R_i and R_e , the Coriolis parameter τ , the Prandtl number P and the magnetic Prandtl number P_m are defined by

$$R_i = \frac{\alpha \gamma \beta d^6}{\nu \kappa}, \quad R_e = \frac{\alpha \gamma \Delta T d^4}{\nu \kappa}, \quad \tau = \frac{2 \Omega d^2}{\nu}, \quad P = \frac{\nu}{\kappa}, \quad P_m = \frac{\nu}{\lambda_0} \quad (2.5)$$

where λ_0 is a typical value of the magnetic diffusivity λ which we allow to vary as a function of the distance r from the center in contrast to the other material properties. Such a variation reflects the often significant variation of the electrical conductivity σ with radius according to the relationship $\lambda = \sigma^{-1} \mu^{-1}$. While $P = 1$ is often assumed with the argument that all effective diffusivities are equal in turbulent media we keep P as a parameter.

Since the velocity field \mathbf{v} as well as the magnetic flux density \mathbf{B} are solenoidal vector fields, the general representation in terms of poloidal and toroidal components can be used,

$$\mathbf{v} = \nabla \times (\nabla \Phi \times \mathbf{r}) + \nabla \Psi \times \mathbf{r}, \quad \mathbf{B} = \nabla \times (\nabla h \times \mathbf{r}) + \nabla g \times \mathbf{r}. \quad (2.6)$$

By multiplying the (curl)² and the curl of equation (6a) by \mathbf{r} we can obtain two equations for Φ and Ψ which will not be given here explicitly (see, for example, Simitev & Busse, 2005). The equations for h and g are obtained through the multiplication of equation (2.4) and of its curl by \mathbf{r} ,

$$[2(1-a)(r-r_i)+a]\nabla^2 L_2 h = P_m [\partial_t L_2 h - \mathbf{r} \cdot \nabla \times (\mathbf{v} \times \mathbf{B})] \quad (2.7)$$

$$[2(1-a)(r-r_i)+a]\nabla^2 L_2 g + 2(1-a)r^{-1}\partial_r(rg) = P_m[\partial_t L_2 g - \mathbf{r} \cdot \nabla \times (\nabla \times (\mathbf{v} \times \mathbf{B}))] \quad (2.8)$$

where the L_2 is defined by

$$L_2 \equiv -r^2 \nabla^2 + \partial_r(r^2 \partial_r)$$

In (2.7) and (2.8) a linear dependence $\lambda = \lambda_0[2(1-a)(r-r_i)+a]$ has been introduced such that $\lambda = \lambda_0$ at the middle of the layer, $r = r_i + 0.5$.

Either rigid boundaries with fixed temperatures as in the benchmark case (Christensen et al., 2001),

$$\Phi = \partial_r(r\Phi) = \Psi = \Theta = 0 \quad \text{at } r = r_i \equiv \eta/(1-\eta) \quad \text{and at } r = r_o \equiv (1-\eta)^{-1}, \quad (2.9)$$

or stress-free boundaries with fixed temperatures,

$$\Phi = \partial_{rr}^2 \Phi = \partial_r(\Psi/r) = \Theta = 0 \quad \text{at } r = r_i \quad \text{and at } r = r_o, \quad (2.10)$$

are frequently used. The latter conditions allow to cover numerically a larger region of the parameter space since the thin Ekman layers at the boundaries are nearly absent. The radius ratio $\eta = 0.4$ is often used in the simulations since it provides a good compromise for the study of both, the regions inside and outside the tangent cylinder. The latter is the virtual cylindrical surface touching the inner spherical boundary at its equator. For the magnetic field it is convenient to employ electrically insulating boundaries such that the toroidal component of the field vanishes there, while the poloidal function h must be matched to the function $h^{(e)}$ which describes the potential fields outside the fluid shell,

$$g = h - h^{(e)} = \partial_r(h - h^{(e)}) = 0 \quad \text{at } r = r_i \quad \text{and at } r = r_o. \quad (2.11)$$

Alternatively an infinitely conducting inner boundary can be assumed,

$$\partial_r g = h = 0 \quad \text{at } r = r_i, \quad (2.12)$$

but computations for the case of an inner boundary with no-slip conditions and an electrical conductivity equal to that of the fluid are also often done. The numerical integration of equations (2.3), (2.7), (2.8), (2.9) and (2.10) together with boundary conditions proceeds most often with the pseudo-spectral method as described by Glatzmaier (1984) and Tilgner (1999) which is based on an expansion of all dependent variables in spherical harmonics for the θ, ϕ -dependences, i.e.

$$\Phi = \sum_{l,m} V_l^m(r, t) P_l^m(\cos \theta) \exp\{im\phi\} \quad (2.13)$$

and analogous expressions for the other variables, Ψ, Θ, h and g . P_l^m denotes the associated Legendre functions. For the r -dependence expansions in Chebychev polynomials are used.

It should be emphasized that the static state $\mathbf{v} = \mathbf{B} = \Theta = 0$ represents a solution of equations (6) for all values of the Rayleigh numbers R_i and R_e , but this solution is unstable except for low or negative values of the latter parameters. Similarly, there exist solutions with $\mathbf{B} = 0$, but $\mathbf{v} \neq 0, \Theta \neq 0$, for sufficiently large values of either R_i or R_e or both, but, again, these solutions are unstable for sufficiently large values of P_m with respect to disturbances with $\mathbf{B} \neq 0$. Dynamo solutions, as all solutions with $\mathbf{B} \neq 0$ and $|\mathbf{B}| \propto r^{-3}$ for $r \rightarrow \infty$ are called, are thus removed by at least two bifurcations from the basic static solution of the problem.

3. Convection in rotating spherical shells

Past research on convection driven dynamo in rotating, self-gravitating spherical shells has shown that the properties of convection in the absence of a magnetic field do change

quantitatively, but not qualitatively after the Lorentz force enters the force balance. It is thus important to understand the properties of non-magnetic convection. A rough idea of the dependence of the critical Rayleigh number R_c for the onset of convection on the parameters of the problem can be gained from the expressions derived from the annulus model (see recent review of Busse, 2002)

$$R_c = 3 \left(\frac{P\tau}{1+P} \right)^{\frac{4}{3}} (\tan \theta_m)^{\frac{8}{3}} r_m^{-\frac{1}{3}} 2^{-\frac{2}{3}}, \quad (3.1a)$$

$$m_c = \left(\frac{P\tau}{1+P} \right)^{\frac{1}{3}} (r_m \tan \theta_m)^{\frac{2}{3}} 2^{-\frac{1}{6}}, \quad \omega_c = \left(\frac{\tau^2}{(1+P)^2 P} \right)^{\frac{1}{3}} 2^{-\frac{5}{6}} (\tan^2 \theta_m / r_m)^{\frac{2}{3}}, \quad (3.1b)$$

where r_m refers to the mean radius of the fluid shell, $r_m = (r_i + r_o)/2$, and θ_m to the corresponding colatitude, $\theta_m = \arcsin(r_m(1 - \eta))$. The azimuthal wavenumber of the preferred mode is denoted by m_c and the corresponding angular velocity of the drift of the convection columns in the prograde direction is given by ω_c/m_c .

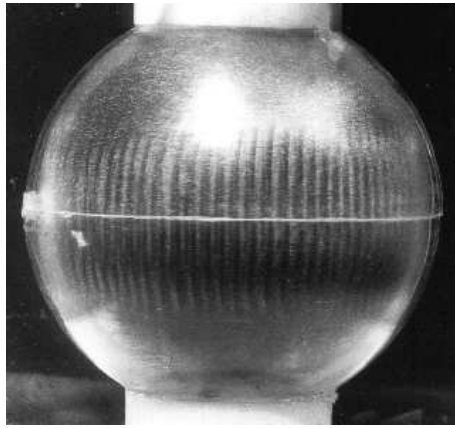


Figure 1. Banana cells in a thin rotating spherical fluid shell cooled from within. Convection driven by centrifugal buoyancy is made visible by a suspension of tiny flakes which become aligned with the shear. Because the inner sphere is cooled, the outer heated, the experiment models the planetary situation where gravity and temperature gradient are reversed since only the product enters force balance. (After Busse & Carrigan, 1976)

While expressions (3.1) correspond to motions in the form of columns aligned with the axis of rotation, convection in the form of “banana cells” is realized in less rapidly rotating or thinner spherical shells as experimentally visualized in figure 1. An analytical theory of the “banana cells” which includes the differential rotation generated by their Reynolds stresses was first derived by Busse (1970). At low Prandtl numbers, namely for $P \lesssim 10/\sqrt{\tau}$ inertial convection in the form of equatorially attached cells becomes prevalent (Ardes et al. 1997; Simitev & Busse, 2003). Its name reflects the fact that it can be described as a small modification of certain inertial waves (Zhang, 1994; Busse & Simitev, 2004). A third form of convection is realized in the polar regions of the shell which are defined as the two fluid domains inside the tangent cylinder. Since gravity and rotation vectors are nearly parallel in these regions (unless $\eta \equiv r_i/r_o$ assumes a value close to unity) convection resembles the kind realized in a horizontal layer heated from below and rotating about a vertical axis. Because the Coriolis force can not largely be balanced by the pressure gradient in this case, the onset of convection is delayed to

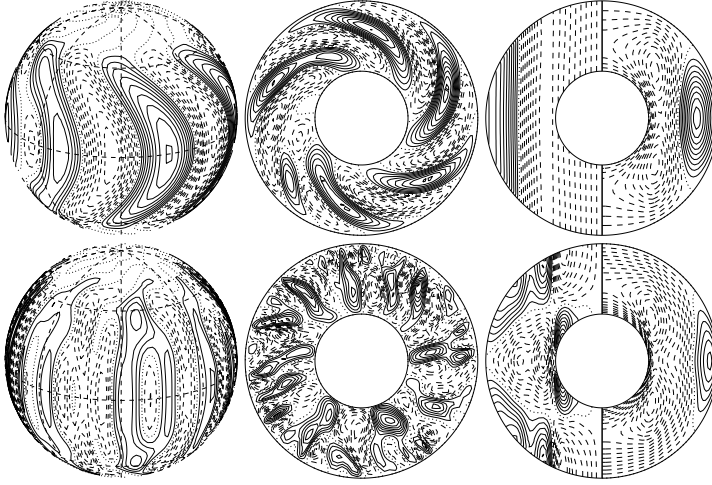


Figure 2. Convection in rotating spherical fluid shells for $\tau = 5 \cdot 10^3$, $R = 2.7 \cdot R_c$, in the cases $P = 0.5$ (upper row, $R = 1.5 \cdot 10^5$) and $P = 20$ (lower row, $R = 4 \cdot 10^5$). Lines of constant u_r in the middle spherical surface, $r = r_i + 0.5$, are shown on the right. The middle plots show streamlines, $r\partial\Phi/\partial\varphi = \text{const.}$, in the equatorial plane. The plots on the right indicate lines of constant mean azimuthal velocity \bar{u}_φ in the left halves and isotherms of $\bar{\Theta}$ in the right halves.

higher values of R where convection outside the tangent cylinder has reached already high amplitudes.

More important than its influence on the onset of convection according to relationships (3.1) is the effect of the Prandtl number on convection at finite amplitudes. Typical features of low and high Prandtl number convection are illustrated in figure 2. The columnar nature of convection does not vary much with P as is evident from the two plots on the left side of the figure. At Prandtl numbers of the order unity or less, - but not in the case of inertial convection-, the convection columns tend to spiral away from the axis and thereby create a Reynolds stress which drives a strong geostrophic differential rotation as shown on the right side of the figure. This differential rotation in turn promotes the spiral tilt and a feedback loop is thus created. At high values of P the Reynolds stress becomes negligible and no significant mean tilt of the convection columns is apparent in the middle plot of the lower row. In this case the differential rotation is generated as a thermal wind caused by the latitudinal gradient of the axisymmetric component of Θ .

The properties of convection are reflected in the averages of the kinetic energy densities of the various components of the velocity field which are defined by

$$\bar{E}_p = \frac{1}{2} \langle |\nabla \times (\nabla \bar{\Phi} \times \mathbf{r})|^2 \rangle, \quad \bar{E}_t = \frac{1}{2} \langle |\nabla \bar{\Psi} \times \mathbf{r}|^2 \rangle, \quad (3.2a)$$

$$\tilde{E}_p = \frac{1}{2} \langle |\nabla \times (\nabla \tilde{\Phi} \times \mathbf{r})|^2 \rangle, \quad \tilde{E}_t = \frac{1}{2} \langle |\nabla \tilde{\Psi} \times \mathbf{r}|^2 \rangle, \quad (3.2b)$$

where the angular brackets indicate the average over the fluid shell and $\bar{\Phi}$ refers to the azimuthally averaged component of Φ , while $\tilde{\Phi}$ is defined by $\tilde{\Phi} = \Phi - \bar{\Phi}$. Analogous definitions hold for the magnetic energy densities where E, Φ etc. are replaced by M, h etc., In figure 3 energy densities have been plotted for convection with and without magnetic fields.

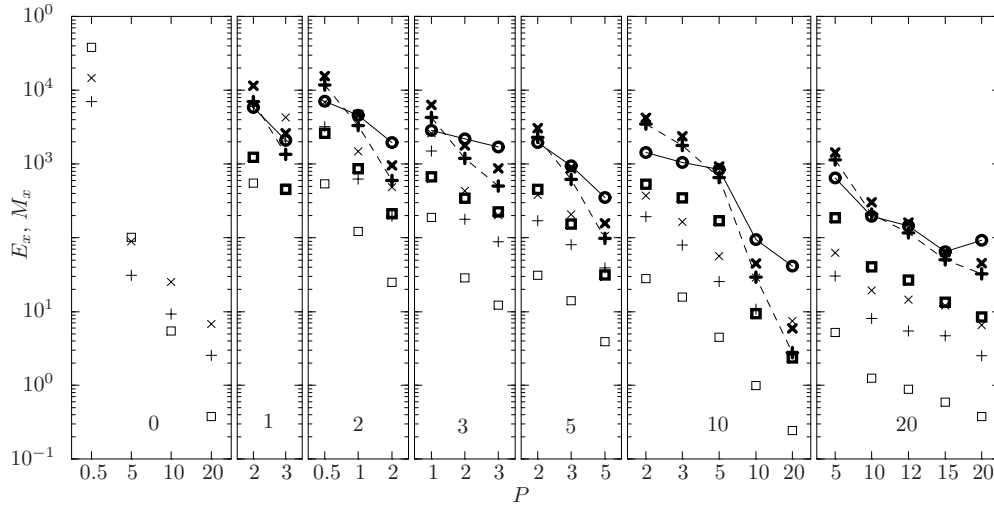


Figure 3. Kinetic (thin symbols) and magnetic (thick symbols) energy densities of convection driven dynamos as function of P for $\tau = 3 \cdot 10^4$, $R = 3.5 \cdot 10^6$, $\eta = 0.4$, $a = 1$ (implying $\lambda \equiv \lambda_0$) and values of P_m as indicated in the boxes. The components $\overline{X}_p, \overline{X}_t, \tilde{X}_p, \tilde{X}_t$ (where $X = E$ or M) are represented by circles, squares, plus-signs and crosses, respectively.

4. Convection driven dynamos

Dynamos are generated by convection in rotating spherical shells for all parameter values as long as the magnetic Reynolds number, $Rm \equiv P_m \sqrt{2E}$ is of the order 50 or higher and the fluid is not too turbulent where the kinetic energy density E is defined by $E = \overline{E}_p + \overline{E}_t + \tilde{E}_p + \tilde{E}_t$. In planetary cores P_m assumes values of the order of 10^{-6} and less, but numerical simulation have achieved so far only values somewhat below 10^{-1} . An important feature demonstrated in figure 3 is the change in the structure of the magnetic field with increasing Prandtl number. While for low values of P the mean poloidal field is small in comparison with the fluctuating components, this situation reverses as P increase. This change is associated with the transition from the geostrophic differential rotation to the thermal wind type differential rotation caused by a latitudinal temperature gradient. While the magnetic energy M may exceed the total kinetic energy E by orders of magnitude in particular for high Prandtl numbers, ohmic dissipation is usually found to be roughly comparable to viscous dissipation or less in numerical simulations. This may be due to the limited numerically accessible parameter space, however.

As long as convection does not occur in the polar regions or is sufficiently weak there, convection outside the tangent cylinder is nearly symmetric with respect to the equatorial plane as is evident from figure 2. As a consequence the dynamo generated magnetic fields exhibit a dipolar or a quadrupolar character unless the non-axisymmetric components by far exceed the axisymmetric components of the field as sometimes happens for high values of Rm or low values of P . In addition dynamos of hemispherical character are often found, for which the field in the northern half is much weaker than in the southern half or vice versa. Quadrupolar and hemispherical dynamos typically oscillate. Dipolar dynamos often oscillate as well, but sometimes these oscillations can not be identified at a distance of a radius or more as is evident in the example of figure 4.

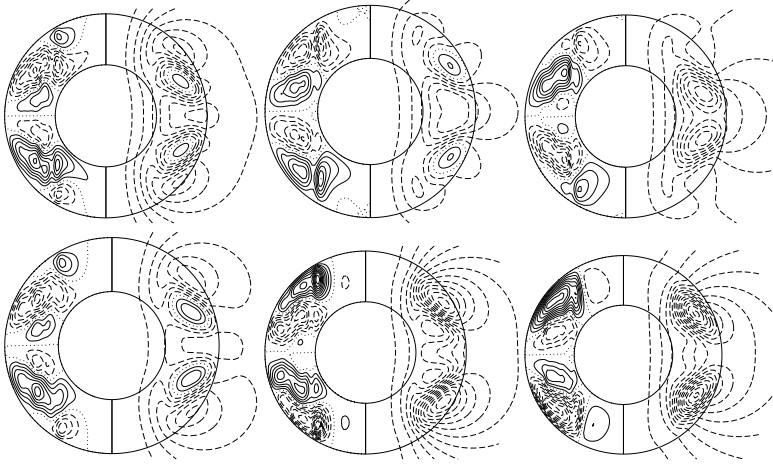


Figure 4. An “invisible” oscillating dynamo in the case of $P = 2$, $\frac{P_m}{P} = 1$, $\tau = 3 \cdot 10^4$, $\eta = 0.5$, $a = 1$ and $R = 2 \cdot 10^6$. The plots show lines of constant B_p in their left halves and meridional field lines, $r \sin \theta \partial_\theta \bar{h} = \text{const.}$, in their right halves. The time sequence of plots starts at the upper left and continues clockwise with $\Delta t = 0.04$ such that a full cycle is completed approximately.

5. Applications to the Giant Planets

It is obvious from the preceding sections that numerical simulations are still far removed from realistic descriptions of dynamo processes in the Giant Planets. There are even more basic issues that need to be resolved. Since the Proudman-Taylor-Theorem holds for barotropic fluids the strong differential rotations observed at the surface of the planets must be expected to continue for a considerable distance into the planetary interiors. Because the poloidal electric current density will be of the order $UB_p\sigma$ where U is a typical zonal velocity, say 100m/s , and B_p measures the strength of the poloidal field the density of Ohmic dissipation becomes of the order $(UB_p)^2\sigma$. When this expression is integrated over a reasonable domain inside the planet it turns out (Liu et al. (2006)) that it exceeds easily the net luminosity of Jupiter as well as that of Saturn when the value of σ for metallic hydrogen is used. Accordingly Liu et al. (2006) argue that the dynamo is located in a region where not only the strong zonal flows penetrating from the surface have been truncated, but where also σ is as small as is compatible with a magnetic Reynolds number of the order of a few 10^2 . Such a region would lie at a depth of less than 15% (35%) of the planetary radius of Jupiter (Saturn) where hydrogen is still a semiconductor (Nellis et al., 1996). A consequence of the latter property is a strong temperature dependence of σ which translates into a high radial increase of λ . It will be of interest to see how these properties and constraints can be accommodated in dynamo simulations producing magnetic fields similar to the observed ones.

The dynamos operating in Uranus and Neptune are similarly constrained (Holme & Bloxham, 1996). Traditionally an ionic electrical conductivity has been assumed for the dynamo regions of these planets, but recent measurements (Lee et al., 2006) indicate that water is semi-conducting under the relevant conditions.

We close with some remarks on the unusual form of the magnetic fields of Uranus and Neptune. The properties that dipole components of the magnetic fields are relatively weak in comparison with other components and that the dipoles are not aligned with the axes of rotation are not especially unusual. Magnetic fields of such character can often be found in simulations of convection driven dynamos. It seems that they are more

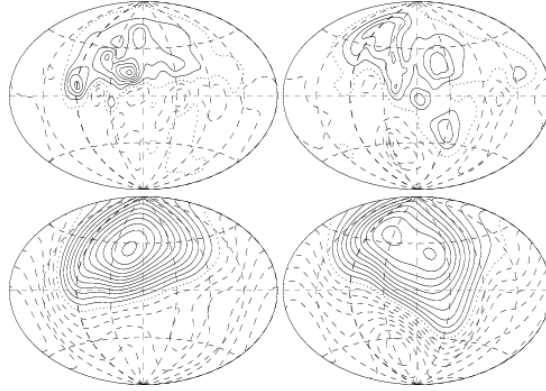


Figure 5. Convection driven dynamos in the cases $P = 0.3, P_m = 2, R_i = 2.5 \cdot 10^6$ (left) and $P = 0.5, P_m = 2.5, R_i = 2.2 \cdot 10^6$ (right). The values $\tau = 3 \cdot 10^4$, $\eta = 0.4$ and $a = 0.2$ are the same in both cases. The plots show lines of constant B_r on the surface $r = r_o + 0.7$ (upper row) and $r = r_o + 1.5$ (lower row)

often found when the diffusivity varies with radius. In figure 6 some typical examples are shown which seem to resemble the observed magnetic fields of the Icy Planets.

References

- Ardes, M., Busse, F. H., & Wicht, J. 1997, *Phys. Earth Plan. Int.* 99, 55
 Burke, B.F. & Franklin, K.L. 1955, *J. Geophys. Res.* 60, 213
 Busse, F. H. 1970, *ApJ* 159, 629
 Busse, F. H. 2002, *Phys. Fluids* 14, 1301
 Busse, F. H., & Carrigan, C. R. 1976, *Science* 191, 81
 Busse, F. H., & Simitev, R. 2004, *J. Fluid Mech.* 498, 23
 Christensen, U.R., Aubert, J., Cardin, P., Dormy, E., Gibbons, S., Glatzmaier, G.A., Grote, E., Honkura, Y., Jones, C., Kono, M., Matsushima, M., Sakuraba, A., Takahashi, F., Tilgner, A., Wicht, J., Zhang, K. 2001, *Phys. Earth Plan. Inter.* 128, 25
 Evonuk, M., & Glatzmaier, G. A. 1991, *Icarus* 181, 458
 Glatzmaier, G. A. 1984, *J. Comp. Phys.* 55, 461
 Holme, R., & Bloxham, J. 1996 *J. Geophys. Res.* 101, 2177
 Lee, K.K.M., Benedetti, L.R., Jeanloz, R., Celliers, P.M., Eggert, J.H., Hicks, D.G., Moon, S.J., Mackinnon, A., Collins, G.W., Henry, E., Koenig, M., & Benuzzi-Mounaix, A. 2006, *J. Chem. Phys.* 125, 014701
 Liu, J., Goldreich, P.M., & Stevenson, D.J. 2006, *Icarus* submitted
 Nellis, W.J., Weir, S.T., & Mitchell, A.C. 1996, *Science* 273, 396
 Ruzmaikin, A.A., & Starchenko, S.V. 1991, *Icarus* 93, 82
 Simitev, R., & Busse, F.H. 2003, *New J. Phys.* 5, 97.1
 Simitev, R., & Busse, F.H. 2005, *J. Fluid Mech.* 532, 355
 Stanley, S., & Bloxham, J. 2004, *Nature* 428, 151
 Tilgner, A. 1999, *Int. J. Numer. Meth. Fluids* 30, 713
 Zhang, K. 1994, *J. Fluid Mech.* 268, 211

Discussion

ANDY INGERSOLL: Jupiter's field is generated so close to the surface, i.e. at $0.86R_J$. Why isn't the field "rougher" at the surface?

F.H. BUSSE: The smoothness depends also on the effective Prandtl numbers P and P_m .